ACS APPLIED MATERIALS & INTERFACES

Research Article

Cite This: ACS Appl. Mater. Interfaces 2019, 11, 31543−31550

www.acsami.org

Layer-Dependent Interfacial Transport and Optoelectrical Properties of MoS_2 on Ultraflat Metals

Hao Lee,[†] Sanchit Deshmukh,[‡] Jing Wen,[§,∥] Viviane Z. Costa,[†] Joachim S. Schuder,[⊥] Michael Sanchez,[⊥] Andrew S. Ichimura,[⊥] Eric Pop,[‡,#,¶] Bin Wang,[§] and A. K. M. Newaz*[,†]

[†]Department of Physics and Astronomy and [⊥]Department of Chemistry and Biochemistry, San Francisco State University, San Francisco, California 94132, United States

[‡]Department of Electrical Engineering, [#]Department of Materials Science and Engineering, and [¶]Precourt Institute for Energy, Stanford University, Stanford, California 94305, United States

[§]School of Chemical, Biological and Materials Engineering, University of Oklahoma, Norman, Oklahoma 73019, United States

[∥]Key Laboratory for Photonic and Electronic Bandgap Materials, Ministry of Education, School of Physics and Electronic Engineering, Harbin Normal University, Harbin 150025, P. R. China

Supporting Information

ABSTRACT: Layered materials based on transition-metal dichalcogenides (TMDs) are promising for a wide range of electronic and optoelectronic devices. Realizing such practical applications often requires metal−TMD connections or contacts. Hence, a complete understanding of electronic band alignments and potential barrier heights governing the transport through metal−TMD junctions is critical. However, it is presently unclear how the energy bands of a TMD align while in contact with a metal as a function of the number of layers. In pursuit of removing this knowledge gap, we have performed conductive atomic force microscopy (CAFM) of few-layered (1 to 5 layers) MoS_2 immobilized on ultraflat conducting Au surfaces [root-mean-square (rms) surface roughness < 0.2 nm] and indium−tin oxide (ITO) substrates (rms surface roughness < 0.7 nm) forming a vertical metal (CAFM tip)−semiconductor−metal device. We have observed that the current increases with the number of layers up to five layers. By applying Fowler−Nordheim tunneling theory, we have determined the barrier heights for different layers and observed how this barrier decreases as the number of layers increases. Using density functional theory calculations, we successfully demonstrated that the barrier height decreases as the layer number increases. By illuminating TMDs on a transparent ultraflat conducting ITO substrate, we observed a reduction in current when compared to the current measured in the dark, hence demonstrating negative photoconductivity. Our study provides a fundamental understanding of the local electronic and optoelectronic behaviors of the TMD−metal junction, which depends on the numbers of TMD layers and may pave an avenue toward developing nanoscale electronic devices with tailored layer-dependent transport properties.

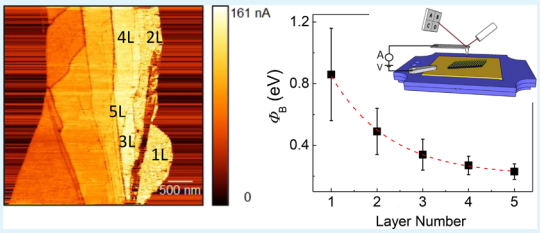

KEYWORDS: *MoS_2, layer dependence, electronic transport, photoconductivity, photoconductive AFM, metal−MoS_2 junction, Schottky barriers, density functional theory*

INTRODUCTION

Layered transition-metal dichalcogenides (TMDs) are van der Waals (vdW) crystals, providing the tantalizing prospect of miniaturizing electronics to truly atomic scales and accelerating the advances of many two-dimensional (2D) optoelectronics.[1−6] These atomically-thin layered TMDs demonstrate some unique properties that include 2D confinement, direct band gap nature,[7] varying band structures with layer thickness,[7−9] and weak screening of charge carriers enhancing the light-matter interactions.[7,8,10] High photon absorption (e.g., for monolayer TMDs, absorption coefficient $\alpha \approx 10\%$ for visible light and $\alpha \approx 40\%$ for ultraviolet photons),[7,11,12] and exciton formation[7,11] make TMDs very attractive for different optoelectronic applications[1,13−17] including sensitive photodetectors,[13,18−20] energy harvesting devices,[21−23] monolayer light-emitting diodes (LEDs),[14,16,17] single photon sources,[24−28] and nanocavity lasers.[29]

Electronic and optoelectronic devices require a metal junction for injection and collection of current. Interfacial charge transport properties play a critical role in governing the current injection or collection in a metal−semiconductor junction. One property that controls charge transport across the junction is the barrier height because of the conduction band offset between the TMD and metal. Although significant progress has been made in demonstrating many different types of TMD-based devices, it is not clear how barrier heights

Received: June 5, 2019
Accepted: July 31, 2019
Published: July 31, 2019

DOI: 10.1021/acsami.9b09868
ACS Appl. Mater. Interfaces 2019, 11, 31543−31550

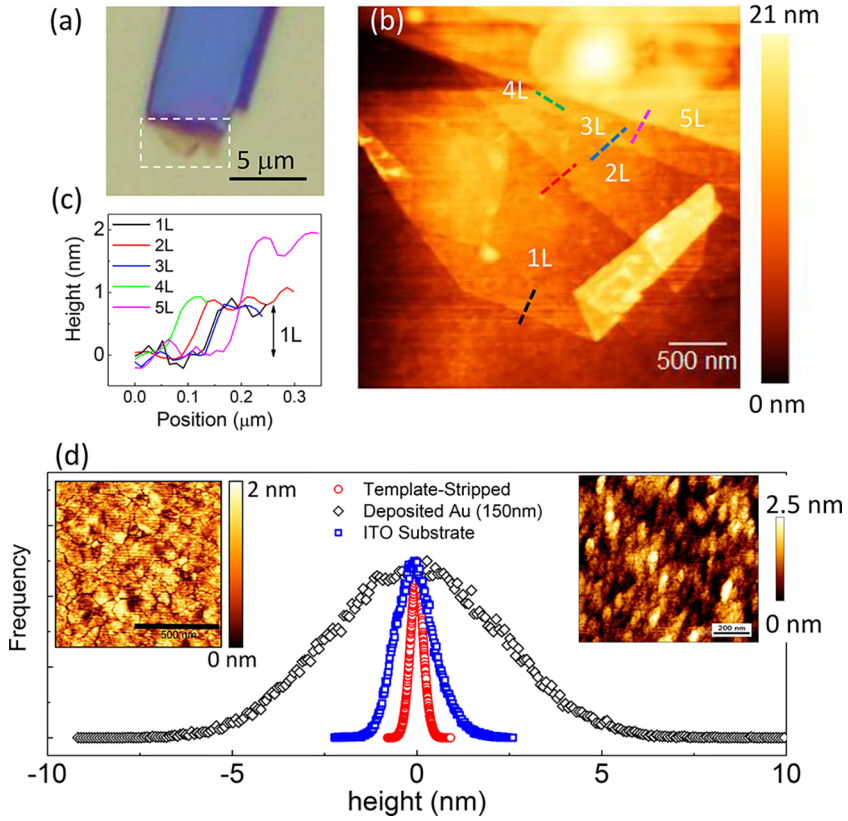

Figure 1. MoS_2 sample on a TS Au substrate. (a) Optical image of a MoS_2 sample. The dotted square region is studied using AFM and CAFM. (b) Height profile AFM image of the marked area (white dotted-square) in (a) measured by the AFM contact mode. The region of different layer numbers is shown. The scale bar is 500 nm. (c) Height profile AFM data extracted along the dashed lines marked in b. (d) Histogram of the height distribution (surface roughness measured by AFM) of the TS Au substrate (TS-Au, ∼150 nm thickness), as the TE-Au substrate of thickness ∼150 nm and the ITO substrate. Au for template stripping was deposited on a single crystal Si wafer. The root-mean-square (rms) value of the surface roughness measured was ∼0.18 nm for TS Au and ∼1.8 nm for the as-deposited substrate. Inset-left: The tapping-mode AFM image of the TS Au surface. Inset-right: the tapping-mode AFM image of 20 nm ITO-coated substrate on a single-crystal quartz substrate. The area of the scanned region is 1 μm × 1 μm. The scale bar is 500 nm for the left image and 200 nm for the right image. A Gaussian fit to the height data provides full-width-half-maxima (fwhm) ∼0.3 nm for the TS Au, ∼5 nm for as-deposited Au, and ∼1 nm for the ITO substrate. The surface roughness profile of template-stripped Au is very similar to surface roughness observed for h-BN (see text).

change with TMD thickness at the few-layer level (1L−5L).[9] One standard technique to elucidate the barrier height is through the measurement of electron affinity by ultraviolet photoelectron spectroscopy (UPS). However, UPS requires a large sample (≥100 μm) which are challenging to prepare for few-layered (1L−5L) MoS_2 by exfoliation.[30,31]

One possible alternative experimental route employs surface probe microscopy (SPM) to study local electrical transport and optoelectronic properties of few-layer TMDs. Because these 2D TMD materials conform to the surface roughness of the substrate, SPM requires that the sample resides on a surface with subnanometer roughness [root-mean-square (rms) surface roughness < 1 nm]. To understand the dependence of the barrier height on TMD layer thickness, we performed conductive atomic force microscopy (CAFM) and photocurrent atomic force microscopy (PCAFM) of few-layer MoS_2 samples immobilized on ultraflat transparent indium−tin oxide (ITO) and template-stripped (TS) Au conducting surfaces.

To probe the layer dependence of interfacial transport properties, CAFM and PCAFM measurements of few-layer MoS_2 samples with thickness varying from a monolayer (1L-MoS_2) to five layers (5L-MoS_2) were performed. To understand the effect of the tip material on the electrical and optical properties, Pt/Ir tips and platinum silicide (Pt/Si) tips were used for both CAFM and PCAFM measurements. Similar results were observed for both Pt/Ir tips and Pt−silicide (Pt/Si) tips. Here, we present the results obtained using Pt/Si tips unless mentioned otherwise. We have studied three MoS_2 samples on the Au substrate and three MoS_2 samples on the ITO-coated substrate. All samples behaved similarly with respect to their electronic and optoelectronic properties. Several important features characteristic of the metal substrate/MoS_2/(Pt/Si) (tip) heterojunctions were observed; (i) the current increases as the layer number increases; (ii) the $I-V$ curve analysis employed Fowler−Nordheim (FN) tunneling theory to give barrier heights that depended on the number of layers; (iii) the barrier height also depends on the type of the conducting substrate; (iv) the current was significantly lower along the edges of the MoS_2 basal plane; and (v) few-layer MoS_2 samples demonstrate negative photoconductivity when illuminated by blue light (460−490 nm). The barrier heights for 1L−5L MoS_2 on the Au(111) surface were calculated with density functional theory (DFT) and followed the observed experimental trends.

RESULTS AND DISCUSSION

Figure 1a,b show an optical image and the corresponding contact-mode AFM height profile image of exfoliated MoS_2 on

DOI: 10.1021/acsami.9b09868
ACS Appl. Mater. Interfaces 2019, 11, 31543−31550

a freshly peeled TS Au surface. The TS Au substrate was prepared following standard procedures[32−35] (see Methods for details). The height profiles of samples were measured mostly by contact-mode AFM. We have also used Raman spectroscopy as an indication of layer thickness, especially when the sample size is larger than the excitation beam diameter (∼1 μm) (see details in the Supporting Information S2). The 1L−5L layer MoS_2 sheet structure is clearly observed in the contact-mode AFM height profile image, Figure 1b,c. Before carrying out CAFM and PCAFM measurements, the rms roughness of the TS-Au and ITO substrates were measured and found to be 0.3 and 0.7 nm, respectively. The ultrasmooth nature of the TS Au surface is very close to the surface roughness of hexagonal boron nitrides (h-BNs),[36] a layered material commonly used as an atomically flat substrate. For comparison, the rms roughness of the external surface of the thermally evaporated (TE) gold layer was ∼2 nm. The metal surface roughness or morphology has an impact on the resistance level of a TMD device.[37] The left and right insets to Figure 1d show tapping-mode height profile images of the TS-Au and ITO-coated surfaces, respectively (see the Supporting Information Figure S1 for an AFM image of a TE-coated AU surface). Figure 1d also compares the height histograms of the TS and TE gold surfaces confirming that template stripping produces a uniformly smooth surface with a narrow full-width-half-maximum (fwhm) distribution while the distribution and roughness of the TE surface are an order of magnitude larger. We have found that employing an ultraflat conducting surface as a substrate for exfoliated TMD is critical to observe consistent electrical and optoelectronic properties of atomically thin MoS_2 crystals.

Now, we discuss the electronic transport behavior of the MoS_2 sample on TS Au substrate. Figure 2a shows schematically the experimental setup used to measure the current under an applied voltage. The bottom inset shows the configuration of the sample with respect to the SiO_2/Si substrate. The MoS_2 sample was directly micro-exfoliated onto the TS Au surface. Figure 2b presents the direct current (dc) map measured with a 0.4 V bias of the sample whose height profile is shown in Figure 1b. The spatial current map clearly demonstrates that the current increases as the layer number increases. This feature becomes clearer in the $I-V$ curves obtained by averaging over a specific layer number as shown in Figure 2c. To compare $I-V$ without the sample, we also performed CAFM measurements of a bare TS Au-substrate and observed a linear $I-V$ for low bias regime and nonlinear behavior for higher bias regime (see the data and analysis in the Supporting Information S3).

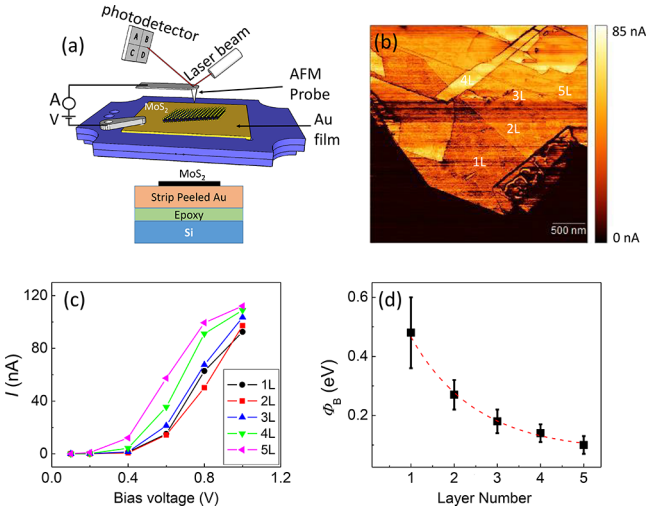

Figure 2. Layer-dependent conductive AFM measurement of the MoS_2 sample on a TS Au substrate. (a) (Top) Schematic diagram of the experimental setup (not to scale) used in CAFM measurements. The current is measured by a current amplifier. (a) (Bottom) Schematic diagram of the sample (see text for details). The MoS_2 sample was directly exfoliated on a TS Au substrate. (b) Conductive AFM data for the sample, whose height profile is shown in Figure 1b. (c) $I-V$ curves for different layers obtained by averaging the current for a flake. (d) Value of the barrier height measured by taking the average of every pixel. The red line is a guide to the eye. The error bar presents the standard deviation of the barrier heights.

Interestingly, almost zero current was observed for the Au substrate outside the MoS_2 flake (Figure 2b). We attribute the nonconducting behavior observed for the gold substrate to the residue left after micro-exfoliation. To determine the reason, we conducted a control CAFM measurement of template stripped Au substrate before and after micro-exfoliation. We have observed that the conducting current drops by ∼4 orders of magnitude (see the Supporting Information). This suggests that the micro-exfoliation process leaves residues and make the metal surfaces nonconducting.

When a metal tip is brought into contact with MoS_2, a Schottky barrier forms, whose height depends on the work function of the Pt/Si tip and the electron affinity of MoS_2.[38−40] In the forward bias regime, high barrier heights suppress thermionic emission, and the barrier thickness is reduced with higher applied bias, which results in tunneling current. On the other hand, the current in the reverse bias is dominated by the thermionic emission above the barrier height. We have presented a detailed analysis of the $I-V$ curve both in the forward bias and reverse bias in the Supporting Information.

The forward biased current can be modeled by the FN tunneling model, which has been widely used to explain the tunneling of an electron between two metals separated by an insulator or semiconductor.[40−43] The tunneling current through a thin semiconductor is given by

$$I(V) = \frac{A_e q^3 m V^2}{8\pi h \Phi_B d^2 m^*} \exp\left(-\frac{8\pi\sqrt{2m^*}\,\Phi_B^{3/2} d}{3hqV}\right) \quad (1)$$

where A_e is the effective contact area, h is Planck's constant, q is the electron charge, d is the thickness of the barrier, Φ_B is the barrier height, m is the electron mass, and m^* is the electron effective mass inside the semiconductor. We used $m^*/m \approx 0.35$ and 0.53 for monolayer MoS_2 and MoS_2 thicker than monolayer (>1L), respectively.[40] If the layer thickness d is known, we can apply eq 1 to determine the barrier height from the $I-V$ curves. More specifically, we replotted the $I-V$ data as $\ln(1/V^2)$ versus $1/V$, whose slope is $\frac{8\pi\sqrt{2m^*}\,\Phi_B^{3/2} d}{3hq}$ and allows measurement of the barrier height. Because the conducting substrate has surface roughness much smaller (∼0.2 nm) than the thickness of monolayer MoS_2 (∼0.65 nm), the separation between the bottom conducting surface and AFM tip remains constant for a specific layer number.

By using a multiple of 1L-MoS_2 (∼0.65 nm) as the layer thickness, the barrier heights for different numbers of layers were calculated as shown in Figure 2d. Interestingly, we observed that the barrier height decreases as the layer number

DOI: 10.1021/acsami.9b09868
ACS Appl. Mater. Interfaces 2019, 11, 31543−31550

increases. This suggests that the current increases as the number of layers increases, which is clearly evident both in the current map in Figure 2b and the $I-V$ curves in Figure 2c. Our observations contrast with the findings of Son et al.,[40] who reported that the barrier height increases as the number of MoS_2 layers increases for a sample immobilized on a rough ITO surface.

To understand the impact of the substrate on the barrier heights, we also studied MoS_2 samples on ultraflat ITO-coated single-crystal quartz substrate. We found that commercially available ITO-coated substrates have high surface roughness and are not suitable for SPM measurement (see Figure S1 for details). The ITO thin films were deposited by physical vapor deposition onto transparent Z-cut quartz substrates (see the Methods section for details). An AFM surface profile image of the substrate is shown in the right inset to Figure 1d. The surface rms roughness of this transparent ITO-coated sample is ~0.7 nm.

The height profile of one MoS_2 sample on the ITO substrate is shown in Figure 3a. The current map for 1L−5L MoS_2 at 1.5 V bias voltage is shown in Figure 3b and clearly shows that the current increases with the increasing layer number. The corresponding $I-V$ curves are shown in Figure 3c, which demonstrate that the current level increases, though minimally compared to MoS_2 on TS-Au, as the layer number increases from 1L to 5L. Note that the current level decreases above five layers. One possible explanation to account for this observation is that the barrier height does not change significantly with the MoS_2 layer number greater than five layers, whereas the sample thickness increases linearly. Hence, the tunneling current decreases significantly as the sample thickness (d) increases as predicted by the FN-tunneling model. Further study is necessary to understand the details of the electrical transport properties of MoS_2 samples thicker than five layers. The FN tunneling theory was used to calculate the barrier heights as shown in Figure 3d. Although the layer number dependence of the barrier height for MoS_2 on ITO is very similar to the samples immobilized on a TS−Au substrate, the barrier height on the ITO substrate is much higher than the barrier heights of MoS_2 on the TS−Au substrate, which is likely caused by different work functions of ITO and Au in the presence of multilayer MoS_2.

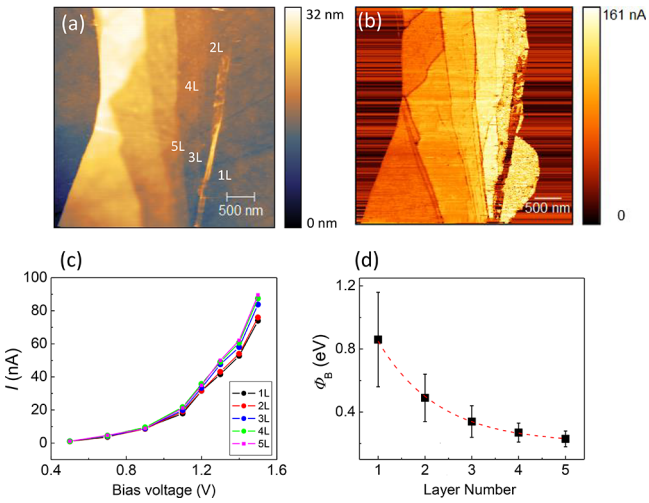

Figure 3. Layer-dependent conductive AFM measurement of the MoS_2 sample on a physical vapor-deposited ITO film. (a) Contact-mode AFM image of the height profile of a sample on the ITO-coated wafer. The layer numbers are shown. The scale bar is 500 nm. (b) Conductive AFM data for the sample for 1.5 V. (c) $I-V$ curves for different layers obtained by averaging the current. (d) Calculated average value of the barrier height measured by taking the average of every pixel. The red line is a guide to the eye. The error bar presents the standard deviation of the barrier heights.

We also studied exfoliated few-layer MoS_2 on TE rough Au substrate and commercially available rough ITO substrates. We could not extract any useful barrier height information because of high surface roughness (see details in the Supporting Information).

Another important feature observed in these MoS_2 samples (both on TS-Au and ITO substrate) is that the edges are less-conducting compared to the middle of the basal plane. The current drops by 2−5 times as the tip approaches the edge compared to regions far from the edges. The low current edges are especially visible, both in Figures 2b and 3b, as dark lines that trace the boundaries between adjacent layers. The current profile along three different edges is presented in Figure S2. Our estimate of the width of that insulating edge is ~20 nm, which is comparable to the Pt/Si tip width. This suggests that the insulating region is smaller than the Pt/Si tip and is beyond our measurement capabilities with our current AFM probe and setup.

To explain our experimental results, DFT calculations were performed to explore the interfacial electronic structure of 1L−5L MoS_2 on an Au(111) surface (Figure 4a). Figure 4b depicts the calculated electron affinity (χ_e) of isolated MoS_2 layers, which shows an increase of the electron affinity (lower conduction band minimum) with the increased layer number. The electron affinity reaches a plateau at about four layers. Figure 4c shows the calculated Schottky barrier, $\phi_B = W - \chi_e$, where W is the work function of Au/MoS_2. The calculated work function is shown in Figure S3 and shows a systematic decrease with layer thickness for the optimized structures. Figure 4c also shows the effect of increasing the interfacial distance between the MoS_2 layers and substrates. The imposed interfacial separation accounts for the possibility that the experimental interfacial spacing may not be exactly the same as the DFT-optimized ones (the black curve in Figure 4c) because of the corrugation of the Au surface and contaminants at the interface. The calculated Schottky barriers for an interlayer spacing of 1−3 Å between Au and MoS_2 shows the general trend of decreasing barrier with the increasing layer number, although ϕ_B reaches a plateau after three layers, which is more in line with the experimental results. Note that the calculated value of monolayer MoS_2 supported on Au in this study is very close to other computational studies.[44,45] The different values of the barrier-height changes between calculations and experiments are likely caused by the challenge to accurately calculate the empty states using DFT, which is a ground-state theory. In addition, the presence of defects in the experimental samples may also lower the barrier height in MoS_2.[46] The increased electron affinity when adding additional layers of MoS_2 is manifested by the downshifted conduction band minimums, which are correlated with the reduced band gap in multilayer MoS_2 as compared to the monolayer.[47]

Finally, we discuss the optoelectronic behavior of the exfoliated 1L−5L MoS_2 sample on an ultraflat ITO substrate. The MoS_2 (1L−5L) samples were immobilized on a transparent ITO substrate. The AFM stage was mounted on an inverted Zeiss microscope. MoS_2 was illuminated through

DOI: 10.1021/acsami.9b09868
ACS Appl. Mater. Interfaces 2019, 11, 31543−31550

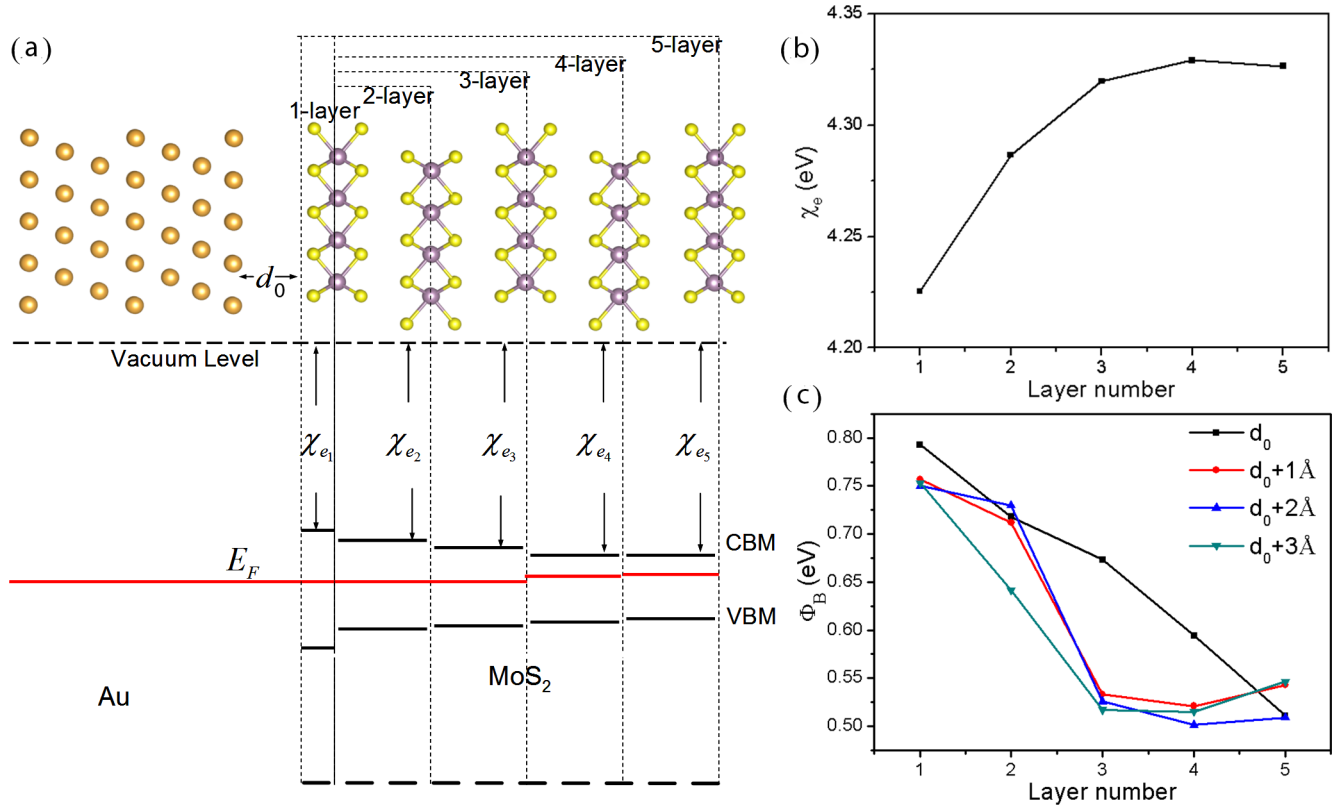

Figure 4. DFT-calculated interfacial electronic structure of Au/MoS_2. (a) Schematic of the MoS_2/Au interface and band alignment. The distance between MoS_2 and Au in the DFT-optimized structure is d_0. (b) DFT-calculated electron affinity of MoS_2 with different thicknesses. (c) DFT-calculated Schottky barrier at the interface of Au/MoS_2 with varied thickness of MoS_2 and interfacial spacing. The black curve shows the values from DFT-optimized structures, while the red, blue, and green ones show the values when the structures are artificially displaced by 1, 2, and 3 Å further away from the Au surface, respectively.

the quartz substrate with an LED source (X-Cite 110), which employed a dichroic filter to select the excitation wavelength range of 460−490 nm. The excitation light was guided by a microscope objective (×20, NA ≈ 0.75) to the sample. The beam area was ∼10 μm with optical power density $P \approx 4$ mW/μm^2. The height profile of the sample is shown in Figure 5a where different layer regions are marked. The corresponding $I-V$ curve for 1L-MoS_2 is shown in Figure 5b. Surprisingly, the current decreases as the sample is illuminated by 460−490 nm photons demonstrating negative photoconductivity. Note that the change in photocurrent (ΔI_{PC}) becomes larger as we increase the bias voltage. The difference in current under illumination ΔI_{PC} ($=I_{light} - I_{dark}$) for V = 1 V is shown as a spatial map in Figure 5c. The spatial map was made by subtracting the AFM current image acquired without illumination from the one illuminated with blue light, and it clearly shows that the current decreased under illumination. Another interesting feature is that ΔI_{PC} is larger for the thicker layer (≥2L) than the monolayer as shown in Figure 5d. The observation of negative photoconductivity of the single-crystal MoS_2 nanosheet is an anomalous photoresponse compared to regular positive photoconductivity behavior observed for planar structured TMDs.[2,4,11,13]

We have also checked the negative photoconductivity of few-layer MoS_2 in a TS Au substrate. We illuminate the sample using a microscope objective underneath the sample in our inverted Zeiss microscope. This requires that the samples reside on a transparent substrate. Moreover, the Au metal layer needs to be thinner to reduce light absorption by Au itself. We

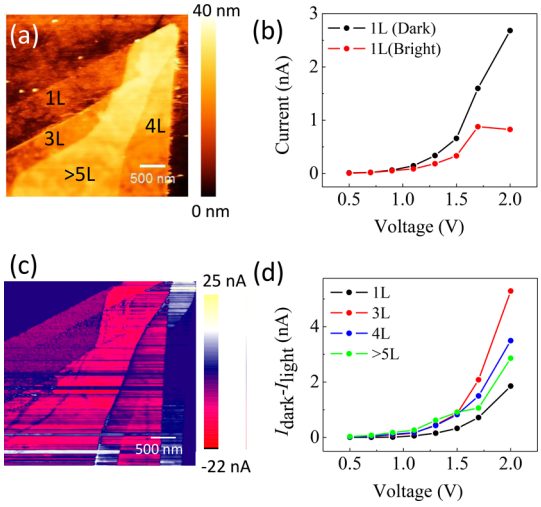

Figure 5. Photoconductive AFM measurement of the sample on an ultraflat ITO-coated single-crystal quartz. (a) Contact-mode AFM image of the height profile of the sample. Different layer regions are marked. The scale bar is 500 nm. (b) IV curve when the sample is illuminated by blue light (black circle) and in the dark (red circle). (c) Photoconductive AFM image of the sample at V = 1 V. The image is obtained by subtracting the illuminated photoconductive AFM image from the conductive AFM image measured in the dark. (d) Voltage-dependent negative photocurrent data ($=I_{dark} - I_{light}$) for different layers.

DOI: 10.1021/acsami.9b09868
ACS Appl. Mater. Interfaces 2019, 11, 31543−31550

prepared a thinner TS Au substrate of 50 nm on a smooth glass substrate and micro-exfoliated few-layer MoS_2. We have observed significant negative photoconductive behavior similar to the few-layer MoS_2 samples on ITO (see the Supporting Information).

Negative photoconductivity of MoS_2 nanosheets connected by two metal electrodes in a planar or horizontal configuration was observed previously, and the effect was attributed to the strong many-body interactions in MoS_2.[48,49] This many-body-related negative photoconductivity in the planar MoS_2 device configuration has transient nature with lifetime on the order of trions (~picoseconds). On the other hand, negative photoconductivity observed in our vertical metal/semiconductor/metal device structure is nontransient or time-independent, which suggests that the origin of negative photoconductivity in our devices is completely different than planar device configurations. One possible explanation is that the excited electron and holes after optical illumination in MoS_2 modify the barrier height, which therefore changes the tunneling current. Strong negative photoconductivity measured across the basal plane suggests that the barrier height increases because of optical illumination, which in turn reduces the tunneling current. Because photoconductivity is a critical parameter applied to optoelectronics, further study is necessary to elucidate the origin of this dc negative photoconductivity. Future work on determining the barrier height at different temperatures and optical powers may help pinpoint the reason behind the negative photoconductivity.

CONCLUSIONS

In conclusion, electrical and optoelectronic properties of 1L–5L MoS_2 samples residing on two different atomically flat conducting surfaces are probed by using CAFM and PCAFM measurements. We observed four important features of electrical and optoelectronic properties of MoS_2 nanosheets measured perpendicular to the basal plane. First, the FN tunneling theory shows that the barrier heights correlate with the number of layers; the barrier height is the highest for the monolayer and then monotonically decreases as the number of layers increases. By using DFT calculations, we attributed this observation to the increase of the electron affinity as the layer number increases. Second, the 1L–5L MoS_2 barrier height depends on the type of the conducting substrate underneath the sample; gold has a lower barrier height than ITO. Third, the edges of MoS_2 are less-conducting than the basal plane. Also fourth, negative dc photoconductivity was observed by illuminating the sample with blue light ($\lambda \approx 460$–490 nm). Our study revealed the interfacial electrical and optoelectronic properties while in contact with an ultraflat conductor and can lead to the development of nanoscale optoelectronic devices with tailored properties.

METHODS

Template-Stripped Gold Substrate. Prime-grade silicon (100) wafers were cleaned with a solution of water, ammonium hydroxide, and 30 wt % hydrogen peroxide in a ratio of 4:1:1 at a temperature of ~70 °C for 10 min (Standard Clean-1). The wafers were then rinsed with copious deionized water, dried under argon, and then placed in a bell jar. The bell jar was evacuated to a base pressure of 10^{-7} Torr, and then, 150 nm of gold was TE onto silicon at a rate of 5 Å/s. After the wafers were removed from the bell jar, precut silicon pieces with dimensions 1 cm × 1 cm were adhered to the gold surface with Devcon 2-Ton Epoxy. To dry epoxy and make strong attachment, the diced wafer/epoxy/deposited-Au-film were kept under pressure for 24 h. The pressure was created by a block of heavy metal (5–7 pounds). Finally, the diced wafer was peeled/stripped using a razor blade. To avoid organic contamination of the freshly peeled gold surface, micro-exfoliated MoS_2 flakes from a bulk sample was transferred by direct contact with the gold surface within ~5 min after template-stripping.

ITO Thin Film Preparation. ITO films were deposited with physical vapor deposition onto transparent Z-cut quartz substrates. The films were sputtered from an as-purchased ITO target in a 10 mTorr Ar ambient at 65 W dc plasma deposition power at room temperature, with a deposition rate ≈ 3 nm/min. In this work, we have employed a 20 nm thick ITO-coated film. The samples were thermally annealed at 400 °C to reduce the sheet resistance (~220 Ω/square).

CAFM and Photoconductive AFM Measurements. CAFM and photocurrent AFM (PCAFM) measurement were conducted using a JPK Nanowizard 4a Bioscience integrated on an inverted Zeiss fluorescence microscope. The JPK conductive AFM module was used to conduct CAFM and PCAFM measurements. The total AFM system was mounted inside a JPK acoustic enclosure, which was also optically opaque. Hence the electrical measurement was conducted in a totally dark environment. For PCAFM measurement, the light was guided by a liquid light guide from an LED light source (X-Cite 110 LED) into a microscope objective (×20, NA ≈ 0.75). The blue illuminating light was filtered by a Zeiss dichroic filter (excitation BP 470/40). AFM images were analyzed and plotted using both Gwyddion software package[50] and JPK data processing software package. The Pt/Si (PtSi-CONT, resonant frequency, $f \approx 13$ kHz, force constants $k \approx 0.2$ N/m) and Pt/Ir (ANSCM-PC, $f \approx 12$ kHz, and $k \approx 0.2$ N/m) probe tips were purchased from NanoAndMore USA and Applied NanoStructures, Inc., respectively.

Raman Characterization. Confocal micro-Raman measurements were performed using commercial equipment (Horiba LabRAM Evolution). A 100× objective lens with a numerical aperture of 0.9 was used. The excitation source was a 532 nm laser (2.33 eV) with an optical power of ~170 μW.

DFT Calculations. The DFT calculations were performed within the framework of the plane-wave method as implemented in the VASP code.[51] The exchange and correlation potential was described by using the generalized gradient approximation in the scheme of the Perdew–Burke–Ernzerhof functional[52] and the projector-augmented wave method[53,54] was employed to give the numerical description of the ion–electron interaction. A cutoff energy of 400 eV was used to limit the plane-wave basis set. The equilibrium distances between the optimized Au substrate and MoS_2 with different layer numbers were determined by calculating the minimums of the energy versus distance curves as relaxed under the stop criterion of 0.03 eV/Å per atom. A vacuum layer of 40 Å has been added to each composite structure of Au and MoS_2 to simulate the surface configuration. The vdW correction based on the Grimme's DFT-D2 method[55] and dipole correction along the direction vertical to the interface have been included to calculate the total energies and electrostatic potentials, which can provide reasonable atomic configurations at the interfaces and vacuum potentials.

ASSOCIATED CONTENT

Supporting Information

The Supporting Information is available free of charge on the ACS Publications website at DOI: 10.1021/acsami.9b09868.

Surface roughness, Raman spectroscopy, transport between the AFM tip and bare Au before, I–V analysis, samples on rough thermally grown Au and commercially available ITO, transport along edges, work function calculations, PCAFM setup, and negative photoconductivity on different metal surfaces (PDF)

DOI: 10.1021/acsami.9b09868
ACS Appl. Mater. Interfaces 2019, 11, 31543–31550

AUTHOR INFORMATION

Corresponding Author

*E-mail: akmnewaz@gmail.com.

ORCID

Jing Wen: 0000-0002-9107-8377
Andrew S. Ichimura: 0000-0002-7826-102X
Eric Pop: 0000-0003-0436-8534
Bin Wang: 0000-0001-8246-1422
A. K. M. Newaz: 0000-0001-8159-1604

Notes

The authors declare no competing financial interest.

ACKNOWLEDGMENTS

The authors acknowledge the support from San Francisco State University (SFSU), the Center for Computing for Life Sciences at SFSU and to the NSF for instrumentation facilities (NSF MRI-CMMI 1626611). H.L., V.Z.C., and A.K.M.N. acknowledge the support from the National Science Foundation Grant ECCS-1708907 and Department of Defense Award (ID: 72495RTREP). The computational research used the supercomputer resources of the National Energy Research Scientific Computing Center (NERSC) and the OU Supercomputing Center for Education & Research (OSCER) at the University of Oklahoma. S.D. and E.P. acknowledge support from the Stanford Non-Volatile Memory Technology Research Initiative (NMTRI) and partial support from SRC grant 2532.001. Part of this work was performed at the Stanford Nano Shared Facility supported by the NSF grant ECCS-1542152.

REFERENCES

(1) Wang, Q. H.; Kalantar-Zadeh, K.; Kis, A.; Coleman, J. N.; Strano, M. S. Electronics and Optoelectronics of Two-Dimensional Transition Metal Dichalcogenides. *Nat. Nanotechnol.* **2012**, *7*, 699−712.

(2) Mak, K. F.; Shan, J. Photonics and Optoelectronics of 2d Semiconductor Transition Metal Dichalcogenides. *Nat. Photonics* **2016**, *10*, 216−226.

(3) Xia, F.; Wang, H.; Xiao, D.; Dubey, M.; Ramasubramaniam, A. Two-Dimensional Material Nanophotonics. *Nat. Photonics* **2014**, *8*, 899−907.

(4) Duan, X.; Wang, C.; Pan, A.; Yu, R.; Duan, X. Two-Dimensional Transition Metal Dichalcogenides as Atomically Thin Semiconductors: Opportunities and Challenges. *Chem. Soc. Rev.* **2015**, *44*, 8859−8876.

(5) Jariwala, D.; Sangwan, V. K.; Lauhon, L. J.; Marks, T. J.; Hersam, M. C. Emerging Device Applications for Semiconducting Two-Dimensional Transition Metal Dichalcogenides. *ACS Nano* **2014**, *8*, 1102−1120.

(6) Manzeli, S.; Ovchinnikov, D.; Pasquier, D.; Yazyev, O. V.; Kis, A. 2D Transition Metal Dichalcogenides. *Nat. Rev. Mater.* **2017**, *2*, 17033.

(7) Mak, K. F.; Lee, C.; Hone, J.; Shan, J.; Heinz, T. F. Atomically Thin MoS_2: A New Direct-Gap Semiconductor. *Phys. Rev. Lett.* **2010**, *105*, 136805.

(8) Splendiani, A.; Sun, L.; Zhang, Y.; Li, T.; Kim, J.; Chim, C.-Y.; Galli, G.; Wang, F. Emerging Photoluminescence in Monolayer MoS_2. *Nano Lett.* **2010**, *10*, 1271−1275.

(9) Howell, S. L.; Jariwala, D.; Wu, C.-C.; Chen, K.-S.; Sangwan, V. K.; Kang, J.; Marks, T. J.; Hersam, M. C.; Lauhon, L. J. Investigation of Band-Offsets at Monolayer−Multilayer MoS_2 Junctions by Scanning Photocurrent Microscopy. *Nano Lett.* **2015**, *15*, 2278−2284.

(10) Britnell, L.; Ribeiro, R. M.; Eckmann, A.; Jalil, R.; Belle, B. D.; Mishchenko, A.; Kim, Y.-J.; Gorbachev, R. V.; Georgiou, T.; Morozov, S. V.; Grigorenko, A. N.; Geim, A. K.; Casiraghi, C.; Neto, A. H. C.; Novoselov, K. S. Strong Light-Matter Interactions in Heterostructures of Atomically Thin Films. *Science* **2013**, *340*, 1311−1314.

(11) Klots, A. R.; Newaz, A. K. M.; Wang, B.; Prasai, D.; Krzyzanowska, H.; Lin, J.; Caudel, D.; Ghimire, N. J.; Yan, J.; Ivanov, B. L.; Velizhanin, K. A.; Burger, A.; Mandrus, D. G.; Tolk, N. H.; Pantelides, S. T.; Bolotin, K. I. Probing Excitonic States in Suspended Two-Dimensional Semiconductors by Photocurrent Spectroscopy. *Sci. Rep.* **2014**, *4*, 6608.

(12) Yalon, E.; Aslan, Ö. B.; Smithe, K. K. H.; McClellan, C. J.; Suryavanshi, S. V.; Xiong, F.; Sood, A.; Neumann, C. M.; Xu, X.; Goodson, K. E.; Heinz, T. F.; Pop, E. Temperature-Dependent Thermal Boundary Conductance of Monolayer MoS_2 by Raman Thermometry. *ACS Appl. Mater. Interfaces* **2017**, *9*, 43013.

(13) Lopez-Sanchez, O.; Lembke, D.; Kayci, M.; Radenovic, A.; Kis, A. Ultrasensitive Photodetectors Based on Monolayer MoS_2. *Nat. Nanotechnol.* **2013**, *8*, 497−501.

(14) Baugher, B. W. H.; Churchill, H. O. H.; Yang, Y.; Jarillo-Herrero, P. Optoelectronic Devices Based on Electrically Tunable P-N Diodes in a Monolayer Dichalcogenide. *Nat. Nanotechnol.* **2014**, *9*, 262−267.

(15) Eda, G.; Maier, S. A. Two-Dimensional Crystals: Managing Light for Optoelectronics. *ACS Nano* **2013**, *7*, 5660−5665.

(16) Ross, J. S.; Klement, P.; Jones, A. M.; Ghimire, N. J.; Yan, J.; Mandrus, D. G.; Taniguchi, T.; Watanabe, K.; Kitamura, K.; Yao, W.; Cobden, D. H.; Xu, X. Electrically Tunable Excitonic Light-Emitting Diodes Based on Monolayer WSe_2 P-N Junctions. *Nat. Nanotechnol.* **2014**, *9*, 268−272.

(17) Sundaram, R. S.; Engel, M.; Lombardo, A.; Krupke, R.; Ferrari, A. C.; Avouris, P.; Steiner, M. Electroluminescence in Single Layer MoS_2. *Nano Lett.* **2013**, *13*, 1416−1421.

(18) Tsai, D.-S.; Liu, K.-K.; Lien, D.-H.; Tsai, M.-L.; Kang, C.-F.; Lin, C.-A.; Li, L.-J.; He, J.-H. Few-Layer MoS_2 with High Broadband Photogain and Fast Optical Switching for Use in Harsh Environments. *ACS Nano* **2013**, *7*, 3905−3911.

(19) Wu, C.-C.; Jariwala, D.; Sangwan, V. K.; Marks, T. J.; Hersam, M. C.; Lauhon, L. J. Elucidating the Photoresponse of Ultrathin MoS_2 Field-Effect Transistors by Scanning Photocurrent Microscopy. *J. Phys. Chem. Lett.* **2013**, *4*, 2508−2513.

(20) Yin, Z.; Li, H.; Li, H.; Jiang, L.; Shi, Y.; Sun, Y.; Lu, G.; Zhang, Q.; Chen, X.; Zhang, H. Single-Layer MoS_2 Phototransistors. *ACS Nano* **2011**, *6*, 74−80.

(21) Tsai, M.-L.; Su, S.-H.; Chang, J.-K.; Tsai, D.-S.; Chen, C.-H.; Wu, C.-I.; Li, L.-J.; Chen, L.-J.; He, J.-H. Monolayer MoS_2 Heterojunction Solar Cells. *ACS Nano* **2014**, *8*, 8317−8322.

(22) Bernardi, M.; Palummo, M.; Grossman, J. C. Extraordinary Sunlight Absorption and One Nanometer Thick Photovoltaics Using Two-Dimensional Monolayer Materials. *Nano Lett.* **2013**, *13*, 3664−3670.

(23) Peng, B.; Ang, P. K.; Loh, K. P. Two-Dimensional Dichalcogenides for Light-Harvesting Applications. *Nano Today* **2015**, *10*, 128−137.

(24) Tonndorf, P.; Schmidt, R.; Schneider, R.; Kern, J.; Buscema, M.; Steele, G. A.; Castellanos-Gomez, A.; van der Zant, H. S. J.; Michaelis de Vasconcellos, S.; Bratschitsch, R. Single-Photon Emission from Localized Excitons in an Atomically Thin Semiconductor. *Optica* **2015**, *2*, 347−352.

(25) Chakraborty, C.; Kinnischtzke, L.; Goodfellow, K. M.; Beams, R.; Vamivakas, A. N. Voltage-Controlled Quantum Light from an Atomically Thin Semiconductor. *Nat. Nanotechnol.* **2015**, *10*, 507−511.

(26) He, Y.-M.; Clark, G.; Schaibley, J. R.; He, Y.; Chen, M.-C.; Wei, Y.-J.; Ding, X.; Zhang, Q.; Yao, W.; Xu, X.; Lu, C.-Y.; Pan, J.-W. Single Quantum Emitters in Monolayer Semiconductors. *Nat. Nanotechnol.* **2015**, *10*, 497−502.

(27) Srivastava, A.; Sidler, M.; Allain, A. V.; Lembke, D. S.; Kis, A.; Imamoğlu, A. Optically Active Quantum Dots in Monolayer WSe_2. *Nat. Nanotechnol.* **2015**, *10*, 491−496.

DOI: 10.1021/acsami.9b09868
ACS Appl. Mater. Interfaces 2019, 11, 31543−31550

(28) Koperski, M.; Nogajewski, K.; Arora, A.; Cherkez, V.; Mallet, P.; Veuillen, J.-Y.; Marcus, J.; Kossacki, P.; Potemski, M. Single Photon Emitters in Exfoliated WSe_2 Structures. *Nat. Nanotechnol.* **2015**, *10*, 503−506.
(29) Wu, S.; Buckley, S.; Schaibley, J. R.; Feng, L.; Yan, J.; Mandrus, D. G.; Hatami, F.; Yao, W.; Vučković, J.; Majumdar, A.; Xu, X. Monolayer Semiconductor Nanocavity Lasers with Ultralow Thresholds. *Nature* **2015**, *520*, 69.
(30) Kadowaki, R.; Sano, N.; Abukawa, T. Peem and Micro-Ups Studies of Cleaved and Exfoliated Molybdenum Disulfide Surfaces. *e-Journal of Surface Science and Nanotechnology* **2017**, *15*, 115−120.
(31) Ogawa, S.; Yamada, T.; Kadowaki, R.; Taniguchi, T.; Abukawa, T.; Takakuwa, Y. Band Alignment Determination of Bulk *h*-BN and Graphene/*h*-BN Laminates Using Photoelectron Emission Microscopy. *J. Appl. Phys.* **2019**, *125*, 144303.
(32) Hegner, M.; Wagner, P.; Semenza, G. Ultralarge Atomically Flat Template-Stripped Au Surfaces for Scanning Probe Microscopy. *Surf. Sci.* **1993**, *291*, 39−46.
(33) Blackstock, J. J.; Li, Z.; Freeman, M. R.; Stewart, D. R. Ultra-Flat Platinum Surfaces from Template-Stripping of Sputter Deposited Films. *Surf. Sci.* **2003**, *546*, 87−96.
(34) Ragan, R.; Ohlberg, D.; Blackstock, J. J.; Kim, S.; Williams, R. S. Atomic Surface Structure of UHV-Prepared Template-Stripped Platinum and Single-Crystal Platinum(111). *J. Phys. Chem. B* **2004**, *108*, 20187−20192.
(35) Lee, S.; Bae, S.-S.; Medeiros-Ribeiro, G.; Blackstock, J. J.; Kim, S.; Stewart, D. R.; Ragan, R. Scanning Tunneling Microscopy of Template-Stripped Au Surfaces and Highly Ordered Self-Assembled Monolayers. *Langmuir* **2008**, *24*, 5984−5987.
(36) Dean, C. R.; Young, A. F.; Meric, I.; Lee, C.; Wang, L.; Sorgenfrei, S.; Watanabe, K.; Taniguchi, T.; Kim, P.; Shepard, K. L.; Hone, J. Boron Nitride Substrates for High-Quality Graphene Electronics. *Nat. Nanotechnol.* **2010**, *5*, 722−726.
(37) English, C. D.; Shine, G.; Dorgan, V. E.; Saraswat, K. C.; Pop, E. Improved Contacts to MoS_2 Transistors by Ultra-High Vacuum Metal Deposition. *Nano Lett.* **2016**, *16*, 3824−3830.
(38) Sze, S. M.; Ng, K. K. *Physics of Semiconductor Devices*, 3rd ed.; Wiley-Interscience: Hoboken, NJ, 2007; p 712.
(39) Rhoderick, E. H. Metal-Semiconductor Contacts. *IEE Proc., Part I: Solid-State Electron Devices* **1982**, *129*, 1.
(40) Son, Y.; Wang, Q. H.; Paulson, J. A.; Shih, C.-J.; Rajan, A. G.; Tvrdy, K.; Kim, S.; Alfeeli, B.; Braatz, R. D.; Strano, M. S. Layer Number Dependence of MoS_2 Photoconductivity Using Photocurrent Spectral Atomic Force Microscopic Imaging. *ACS Nano* **2015**, *9*, 2843−2855.
(41) Ahmed, F.; Choi, M. S.; Liu, X.; Yoo, W. J. Carrier Transport at the Metal−MoS_2 Interface. *Nanoscale* **2015**, *7*, 9222−9228.
(42) Hattori, Y.; Taniguchi, T.; Watanabe, K.; Nagashio, K. Determination of Carrier Polarity in Fowler−Nordheim Tunneling and Evidence of Fermi Level Pinning at the Hexagonal Boron Nitride/Metal Interface. *ACS Appl. Mater. Interfaces* **2018**, *10*, 11732−11738.
(43) Lee, S.; Choi, K.-Y.; Lee, S.; Park, B. H.; Park, J.-G. Tunneling Transport of Mono- and Few-Layers Magnetic Van Der Waals $MnPS_3$. *APL Mater.* **2016**, *4*, 086108.
(44) Zhong, H.; Quhe, R.; Wang, Y.; Ni, Z.; Ye, M.; Song, Z.; Pan, Y.; Yang, J.; Yang, L.; Lei, M.; Shi, J.; Lu, J. Interfacial Properties of Monolayer and Bilayer MoS_2 Contacts with Metals: Beyond the Energy Band Calculations. *Sci. Rep.* **2016**, *6*, 21786.
(45) Gong, C.; Colombo, L.; Wallace, R. M.; Cho, K. The Unusual Mechanism of Partial Fermi Level Pinning at Metal−MoS_2 Interfaces. *Nano Lett.* **2014**, *14*, 1714−1720.
(46) McDonnell, S.; Addou, R.; Buie, C.; Wallace, R. M.; Hinkle, C. L. Defect-Dominated Doping and Contact Resistance in MoS_2. *ACS Nano* **2014**, *8*, 2880−2888.
(47) Kwon, J.; Lee, J.-Y.; Yu, Y.-J.; Lee, C.-H.; Cui, X.; Hone, J.; Lee, G.-H. Thickness-Dependent Schottky Barrier Height of MoS_2 Field-Effect Transistors. *Nanoscale* **2017**, *9*, 6151−6157.
(48) Lui, C. H.; Frenzel, A. J.; Pilon, D. V.; Lee, Y.-H.; Ling, X.; Akselrod, G. M.; Kong, J.; Gedik, N. Trion-Induced Negative Photoconductivity in Monolayer MoS_2. *Phys. Rev. Lett.* **2014**, *113*, 166801.
(49) Lu, J.; Liu, H.; Sun, J. Negative Terahertz Photoconductivity in 2D Layered Materials. *Nanotechnology* **2017**, *28*, 464001.
(50) Nečas, D.; Klapetek, P. Gwyddion: An Open-Source Software for Spm Data Analysis. *Cent. Eur. J. Phys.* **2012**, *10*, 181−188.
(51) Kresse, G.; Furthmüller, J. Efficient Iterative Schemes for Ab Initio Total-Energy Calculations Using a Plane-Wave Basis Set. *Phys. Rev. B: Condens. Matter Mater. Phys.* **1996**, *54*, 11169−11186.
(52) Perdew, J. P.; Burke, K.; Ernzerhof, M. Generalized Gradient Approximation Made Simple. *Phys. Rev. Lett.* **1996**, *77*, 3865−3868.
(53) Blöchl, P. E. Projector Augmented-Wave Method. *Phys. Rev. B: Condens. Matter Mater. Phys.* **1994**, *50*, 17953−17979.
(54) Kresse, G.; Joubert, D. From Ultrasoft Pseudopotentials to the Projector Augmented-Wave Method. *Phys. Rev. B: Condens. Matter Mater. Phys.* **1999**, *59*, 1758−1775.
(55) Grimme, S.; Antony, J.; Ehrlich, S.; Krieg, H. A Consistent and Accurate Ab Initio Parametrization of Density Functional Dispersion Correction (Dft-D) for the 94 Elements H-Pu. *J. Chem. Phys.* **2010**, *132*, 154104.

DOI: 10.1021/acsami.9b09868
ACS Appl. Mater. Interfaces 2019, 11, 31543−31550

Supporting Information:

Layer dependent Interfacial Transport and Optoelectrical properties of MoS_2 on Ultra-flat metals

Hao Lee[1], S. Deshmukh[2], Jing Wen[3,4], V.Z. Costa[1], J. S. Schuder[5], M. Sanchez[5], A. Ichimura[5], Eric Pop[2,6,7], Bin Wang[3], and A. K. M. Newaz[1,*]

[1]Department of Physics and Astronomy, San Francisco State University, San Francisco, California 94132, USA

[2]Department of Electrical Engineering, Stanford University, Stanford, California 94305, USA

[3]School of Chemical, Biological and Materials Engineering, University of Oklahoma, Norman, Oklahoma 73019, United States

[4]Key Laboratory for Photonic and Electronic Bandgap Materials, Ministry of Education, School of Physics and Electronic Engineering, Harbin Normal University, Harbin 150025, P. R. China

[5]Department of Chemistry and Biochemistry, San Francisco State University, San Francisco, California 94132, USA

[6]Department of Materials Science and Engineering, Stanford University, Stanford, California 94305, USA

[7]Precourt Institute for Energy, Stanford University, Stanford, California 94305, USA

[*]Email:akmnewaz@gmail.com

S1. TE-Au surface roughness

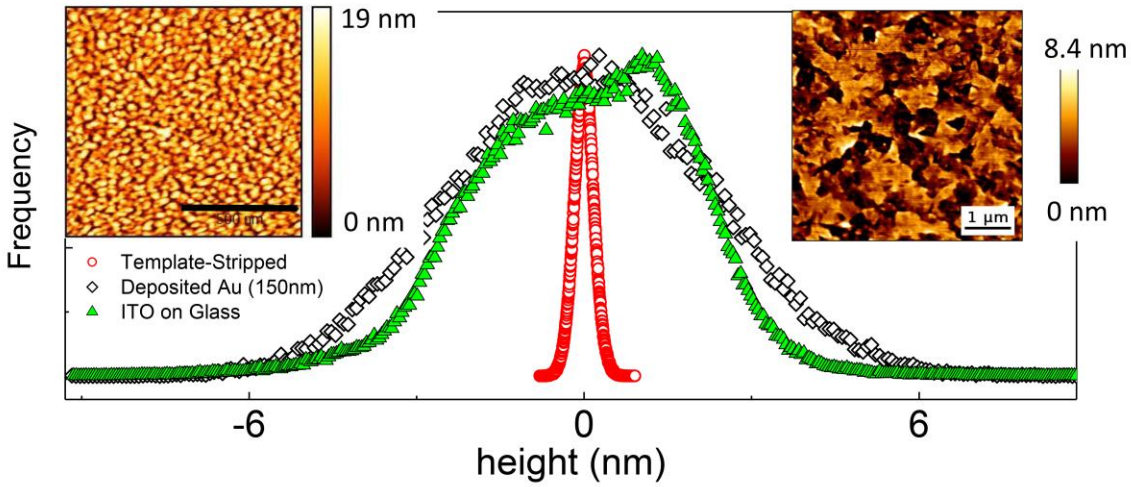

Figure S1: Surface roughness of thermally evaporated Au substrate and commercially available ITO on a glass substrate (Delta Technologies). Main panel: histogram of the height distribution (surface roughness measured by AFM) of the template-stripped Au substrate (red circle), as thermally evaporated Au (black square) substrate of thickness ~150 nm and commercial ITO on a glass substrate (green triangle). The root mean squared (RMS) value of the surface roughness measured was ~ 0.18 nm for template-stripped Au and ~1.8 nm for as-deposited Au substrate and ~1.9 nm for ITO on a glass substrate. Inset-left: tapping mode AFM image of the thermally evaporated Au surface. Inset-right: tapping mode AFM image ITO coated glass substrate. A Gaussian fit to the height data provides full width at half maxima (FWHM) ~ 0.3 nm for the template-stripped Au, ~ 5 nm for as-deposited Au and ~ 4 nm for the ITO substrate.

S2. Layer number determination by Raman Spectroscopy.

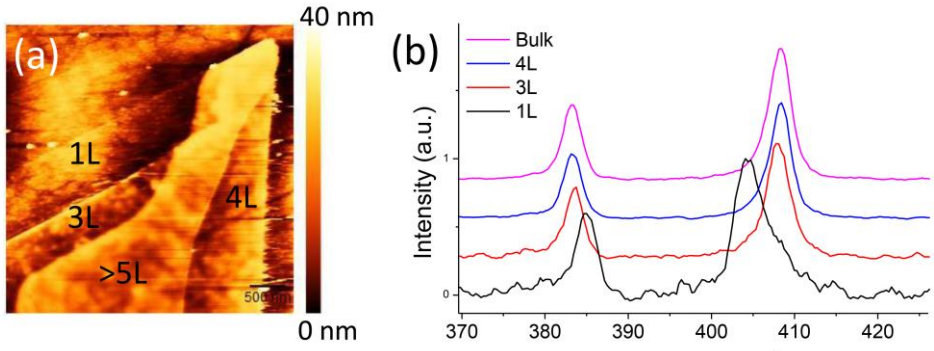

Figure S2: Raman based layer number determination. (a) AFM height profile of few layer MoS_2 on a ultra-flat ITO. The scale bar is 500 nm (b) Raman spectroscopy data for different layers. Here we define bulk as 5L or more layers MoS_2.

S3. Electronic transport between metallic AFM tip and bare Au substrate

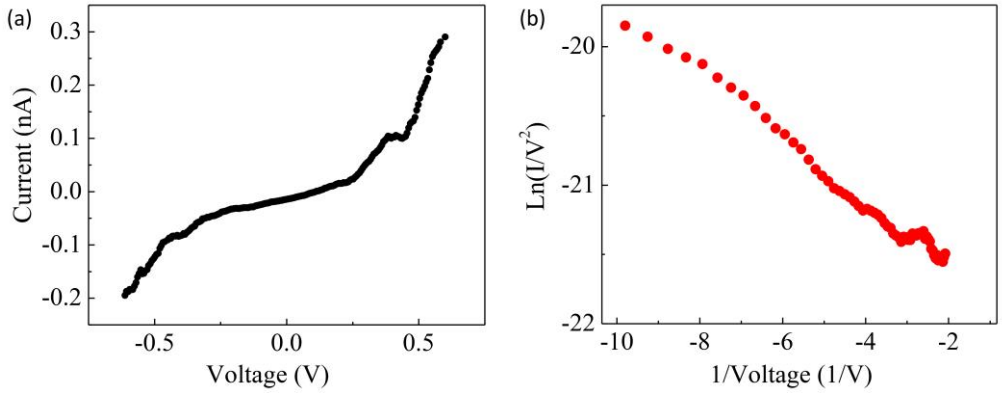

Figure S3: I-V curve for a bare template-stripped Au substrate. (a) Measured I-V curve. (b) $\ln(\frac{I}{V^2}) - 1/V$ plot for the data shown in (a) . The linear behavior suggests a tunneling current between the AFM tip and bare Au substrate.

S4. Electronic transport between metallic AFM tip and bare Au substrate after exfoliation

We observed that the current is vanishingly small outside the MoS_2 sample as in Fig.2 and Fig.3 main text. To determine the reason, we conducted a control CAFM measurements of template stripped Au-substrate before and after the micro-exfoliation. We have observed that the conducting current drops by ~4 orders of magnitude after exfoliating the samples as shown in Figure S4. This suggests that the micro-exfoliation leaves residues and make the metal surfaces non-conducting.

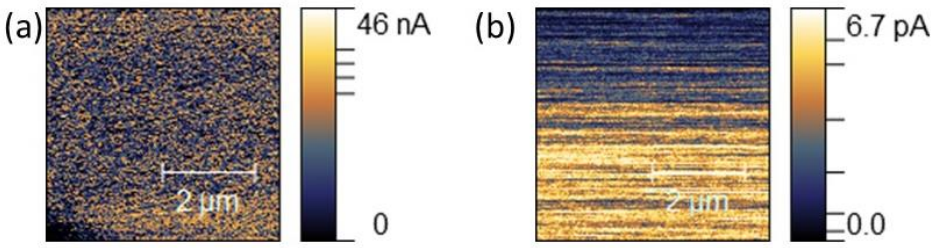

Figure S4: CAFM measurement of a template stripped-Au substrate before exfoliation (a) and after exfoliation (b). Note that the current drops by ~4 orders due to the exfoliation. The measurements were taken at 0.7 V for both cases.

S5: *I-V* analysis in the forward bias regime and the negative bias regime

To determine the electronic transport mechanism governing the *I-V* curve, we prepared 1L-MoS_2 and 2L-MoS_2 sample on template-stripped Au substrate. We measured I-V curve using the voltage spectroscopy mode (also known as cyclic voltammetry mode) of the CAFM measurements provided by the AFM manufacturer (JPK). The experimentally

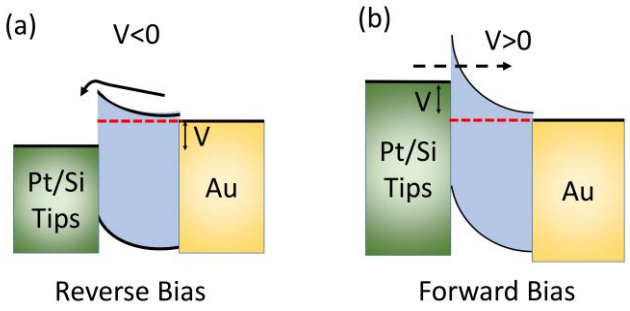

Figure S5: (a) Schematic band diagram of a thin MoS_2 and Pt-Silicide tip junction under reverse bias. (b) Schematic band diagram of a thin MoS_2 and Pt-Silicide tip junction under forward bias.

measured *I-V* curves for 1L-MoS_2 and 2L-MoS_2 are presented in Fig.S6 (a-b). We observed that the *I-V* curves in the forward bias regime and reverse bias regime are not symmetric, which suggests that the different transport mechanisms are determining the current through our vertical structures. We present schematic band structures of Pt-Silicide/MoS_2/Au in Fig.S5. When a metal tip is brought into contact with MoS_2, a Schottky barrier forms, whose height depends on the work function of Pt-Silicide tip and the electron affinity of MoS_2.[1-3]

In the forward bias regime (Fig.S5-b), high barrier height suppresses the thermionic emission and the barrier thickness is reduced with higher applied bias, which results in a tunneling current. This forward current can be modeled by FN tunneling model, which has been widely used to explain the tunneling of an electron between two metals separated by an insulator or semiconductor.[3-6] The tunneling current through a thin semiconductor is given by

$$I(V) = \frac{A_e q^3 m V^2}{8\pi h \Phi_B d^2 m^*} \exp\left(-\frac{8\pi\sqrt{2m^*}\Phi_B^{3/2} d}{3hqV}\right) \quad (1)$$

where A_e is the effective contact area, h is Planck's constant, q is the electron charge, d is the thickness of the barrier, Φ_B is the barrier height, m is the electron mass, and m^* is the electron effective mass inside the semiconductor. We used $\frac{m^*}{m} \sim 0.35$ and 0.53 for monolayer MoS_2 and bulk MoS_2 (>1L), respectively.[3] Our fitting for 1L-MoS_2 and 2L-MoS2 are shown in Fig.S6(a-b), which shows an excellent agreement. The above equation (1) suggests that FN tunneling results a linear $\ln\frac{I}{V^2}$ versus $1/V$ plot. Indeed, we observed that $\ln\frac{I}{V^2}$ varies linearly as a function of $1/V$, as shown in the Fig. S6(b) and Fig.6(e) for 1L-MoS_2 and 2L-MoS_2, respectively. But, in the reverse bias regime, we observed that $\ln\frac{I}{V^2}$ varies non-linearly as a function of 1/V as shown in Fig.S6(c) and Fig.S6(f) for 1L-MoS_2 and 2L-MoS_2, respectively. Hence *I-V* behavior in the forward and reverse bias regime confirms that the current in the forward bias is determined by the FN tunneling and the current in the reverse bias is not due to FN tunneling.

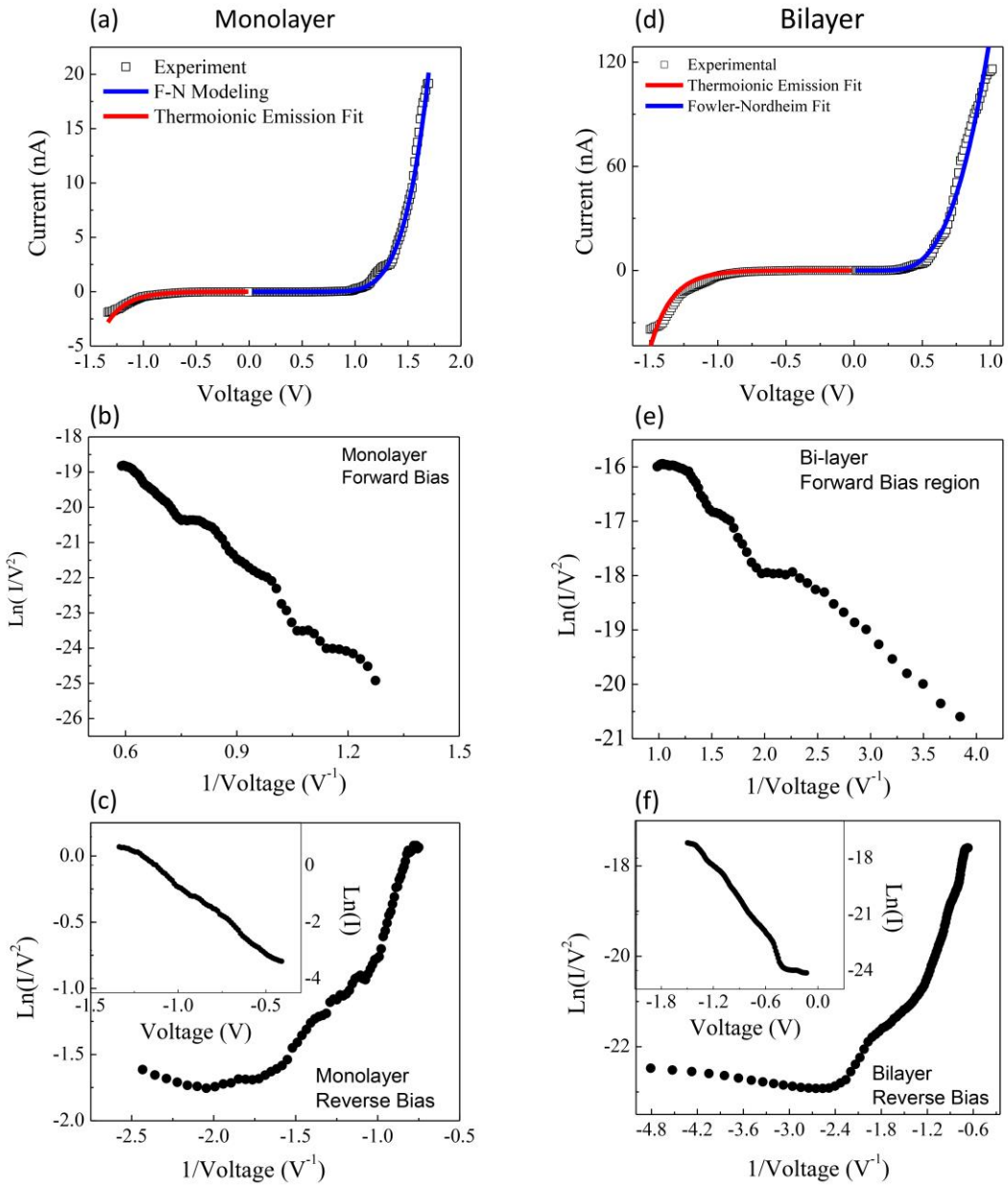

Figure S6: Current-voltage (I-V) measurement and the analysis of a 1L-MoS_2 (Left row) and 2L-MoS_2 (right row). Fig.(a) and (d) presents the *I-V* curve and the fitting for 1L-MoS_2 and 2L-MoS_2 samples, respectively. The square presents the current voltage *(I-V)* curve obtained by CAFM measurements. The reverse bias region is fit by a thermionic emission model (red line) while the forward bias region is fit by a Fowler-Nordheim (FN) tunneling model (blue line). Fig.(b) and (e) present the linear behavior of $ln\frac{1}{V^2}$ -$1/V$ plot in the forward bias regime, which suggests that the current is due to FN tunneling. Fig.(c) and Fig.(f) present the plot $ln\frac{1}{V^2}$ -$1/V$ in the reverse bias regime. The inset of the plots Fig.(c) and Fig.(f) are showing the linear behavior of the $ln\, I - V$ plot, which suggests that the current is due to thermionic emission.

In the reverse bias regime, we use thermionic emission model to model our *I-V* behavior, which was also used before in explaining the charge transport through MoS_2 layers.[3, 7] The current due to thermionic emission model[1] is given by

$$I = I_0\left[e^{\frac{qV}{\eta k_B T}} - 1\right] \qquad (2)$$

where η is known as the ideality factor and I_o is called the saturation current, which is given by

$$I_0 = A_e A^* T^2 e^{-\frac{q\Phi_B}{k_B T}} \qquad (3)$$

Here A_e denotes the effective contact area. Eq.(2) suggests that $\ln I$ will vary linearly as a function of the voltage due to the thermionic equation. Indeed, we have observed a linear behavior in the $\ln I$ vs V plot as shown in the inset of Fig.S6(c) and Fig.S6(f) for 1L-MoS_2 and 2L-MoS_2, respectively. This confirms that the current in the reverse bias is due to thermionic emission.

S6: MoS_2 on rough thermally grown Au and commercially available ITO

We have also studied few-layers MoS_2 exfoliated on thermally grown rough Au substrate and commercially available ITO. The height profile and the current mapping of a monolayer MoS_2 sample on rough Au surface are shown in Fig.7(a-b) and Fig.7c, respectively. We note that the height profile of the sample varies over several nanometers. Local height variations will introduce straining effect and may modify the transport measurements.[8, 9] The height profile of MoS2 sample on a commercially available ITO substrate is shown in Fig.7(d).

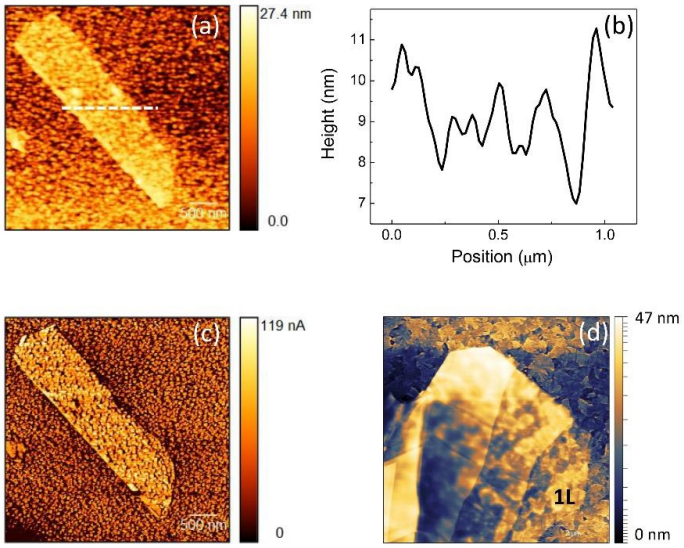

Figure S7: MoS_2 samples on rough substrate. (a) Height profile AFM measurement of a monolayer MoS_2 sample on thermally grown Au substrate. (b) Height profile along the white dashed line in Fig.(a). (c) The spatial current mapping of the sample presented in Fig.1(a). (d) The height profile of the a few layer MoS_2 sample on a commercially available ITO substrate.

S7. Electronic transport along the edges

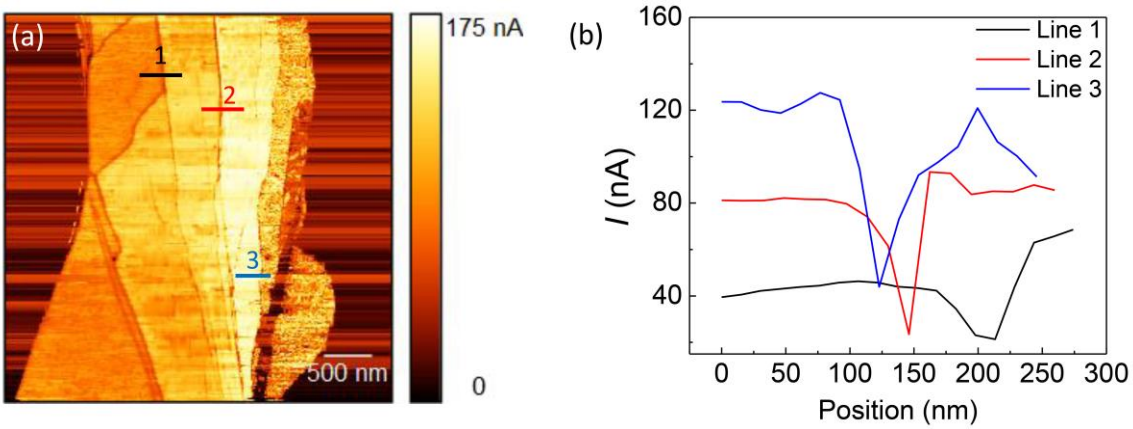

Figure S8: (a) Left is presenting the current map of MoS_2 sample on an ITO substrate. The current is measured at 1.3 V. Three lines of different (black, red and blue) are marked whose current profiles are presented in Fig. (b).

S8. Work function calculations

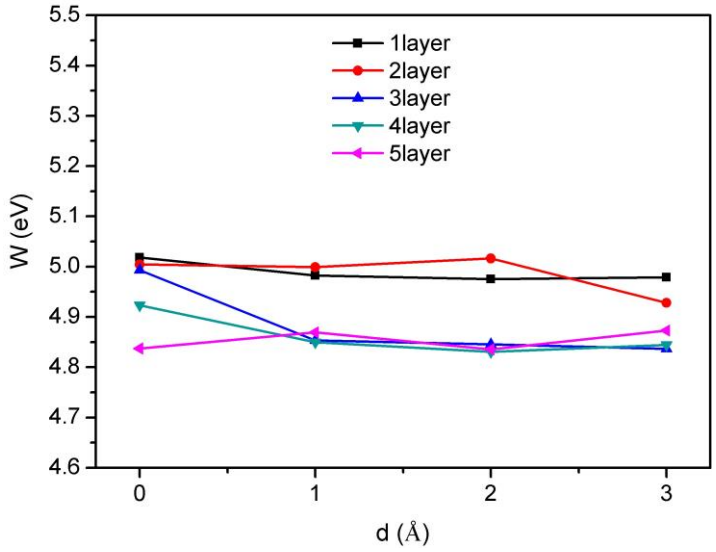

Figure S9. Calculated work function of MoS_2 on Au as a function of the thickness of MoS_2 and the interfacial spacing between the first layer of MoS_2 and the Au (111) surface. This work function has been used to calculate the Schottky barrier in Figure 4c in the main text.

S9: Photoconductive AFM measurements setup

The experimental setup of the photoconductive AFM measurements is shown in Fig.S9.

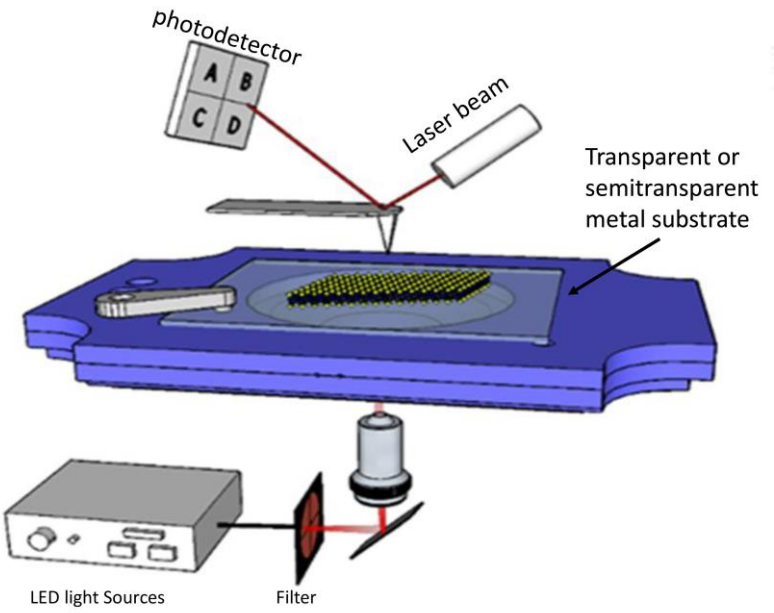

Figure S9: Photoconductive AFM measurements. Filters were used to select the color of the excitation light. Few-layer MoS_2 samples were prepared on transparent or semitransparent substrate to ensure high light transmission.

S10: Negative photoconductivity of few layer MoS_2 on different metal surfaces

We studied the negative photoconductivity of few layer MoS_2 samples on rough Ito surfaces and template stripped Au surfaces. The results is shown in figure S10.

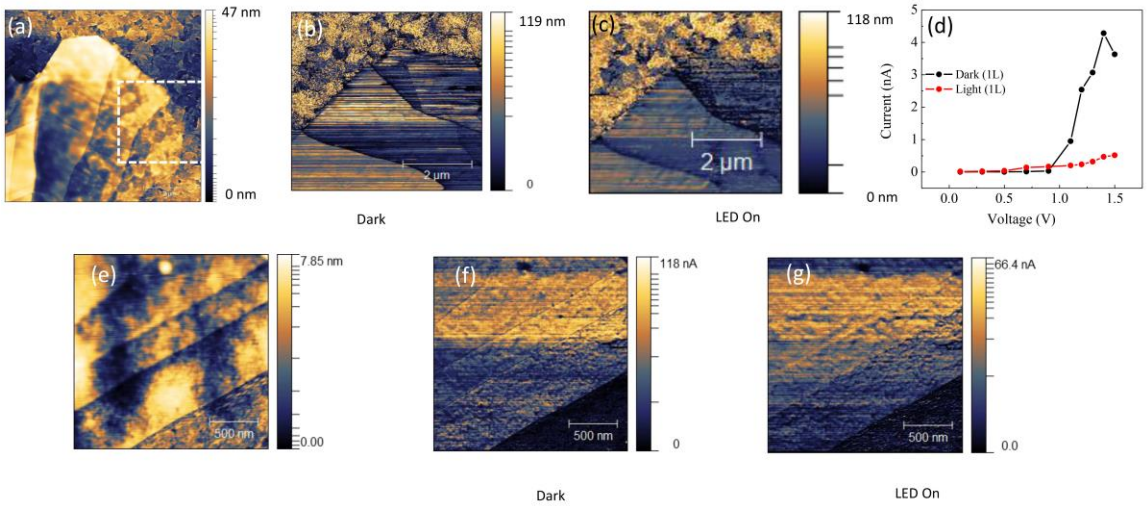

Figure S10: Negative photoconductivity of few layer MoS_2 on commercially available rough ITO surface (Fig.a-d) and template stripped Au-surfaces (Fig.e-g). Fig(a) presents the surface profile of the ITO surface. CAFM measurements of few layer MoS_2 sample with light and without light are presented in Fig.(b) and Fig.(c), respectively. The data were recorded for samples under bias 1.5V. Voltage dependence current data is presented in Fig.(d). (e) The height profile AFM image of a MoS_2 sample directly exfoliated on a template stripped Au surface. To ensure light transmission, the template stripped Au substrate was prepared on a glass substrate.

References:

1. Sze, S. M.; Ng, K. K. *Physics of Semiconductor Devices*. 3rd ed.; Wiley-Interscience: Hoboken, N.J., 2007; p 712
2. Rhoderick, E. H. Metal-Semiconductor Contacts. *IEE Proceedings I - Solid-State and Electron Devices* **1982**, 129, 1.
3. Son, Y.; Wang, Q. H.; Paulson, J. A.; Shih, C.-J.; Rajan, A. G.; Tvrdy, K.; Kim, S.; Alfeeli, B.; Braatz, R. D.; Strano, M. S. Layer Number Dependence of Mos_2 Photoconductivity Using Photocurrent Spectral Atomic Force Microscopic Imaging. *ACS Nano* **2015**, 9, 2843-2855.
4. Ahmed, F.; Choi, M. S.; Liu, X.; Yoo, W. J. Carrier Transport at the Metal–Mos2 Interface. *Nanoscale* **2015**, 7, 9222-9228.
5. Hattori, Y.; Taniguchi, T.; Watanabe, K.; Nagashio, K. Determination of Carrier Polarity in Fowler–Nordheim Tunneling and Evidence of Fermi Level Pinning at the Hexagonal Boron Nitride/Metal Interface. *ACS Applied Materials & Interfaces* **2018**, 10, 11732-11738.
6. Lee, S.; Choi, K. Y.; Lee, S.; Park, B. H.; Park, J. G. Tunneling Transport of Mono- and Few-Layers Magnetic Van Der Waals Mnps3. *Apl Mater* **2016**, 4.
7. Li, Y.; Xu, C.-Y.; Zhen, L. Surface Potential and Interlayer Screening Effects of Few-Layer Mos2 Nanoflakes. *Appl. Phys. Lett.* **2013**, 102, 143110.
8. Conley, H. J.; Wang, B.; Ziegler, J. I.; Haglund, R. F.; Pantelides, S. T.; Bolotin, K. I. Bandgap Engineering of Strained Monolayer and Bilayer Mos2. *Nano Lett.* **2013**, 13, 3626-3630.
9. English, C. D.; Shine, G.; Dorgan, V. E.; Saraswat, K. C.; Pop, E. Improved Contacts to Mos2 Transistors by Ultra-High Vacuum Metal Deposition. *Nano Lett.* **2016**, 16, 3824-3830.